

Spatiotemporal high-resolution mapping of biological production in the Southern Ocean

Xianliang L. Pan^{1✉}, Xiangxing Lai¹, Ryosuke Makabe², Daisuke Hirano² & Yutaka W. Watanabe³

The Southern Ocean is considered to play an important role in the global biogeochemical cycles of carbon and nutrients. It is still unclear how biological production there impacts climate change owing to the remarkable gap between the current and the ideal state of research. Here, we proposed a new concept of combining Neural Network based parameterization of dissolved inorganic carbon with Biogeochemical Argo floats, showing simultaneously spatiotemporal distributions of net community production and resupply of carbon from the deep ocean based on the dissolved inorganic carbon change. It indicated a total net community production of 4.1 ± 0.3 Pg-C year⁻¹ over the Southern Ocean, which accounts for 45% of global annual oceanic carbon export and is 20% higher than the previous estimates. Furthermore, net community production in the Southern Ocean has decreased by 0.8% year⁻¹ since the 2010s, indicating that it may be contributing as positive feedback to global warming.

¹ Graduate School of Environmental Science, Hokkaido University, Sapporo, Japan. ² National Institute of Polar Research, Tokyo, Japan. ³ Faculty of Environmental Earth Science, Hokkaido University, Sapporo, Japan. ✉email: panxianliang@ees.hokudai.ac.jp

Model simulations predict that the Southern Ocean (SO, south of 30°S) accounts for more than 40% of the total anthropogenic carbon dioxide (CO₂) uptake into the ocean, despite accounting for approximately 30% of the total ocean surface area¹. The SO is currently considered an important region in the global biogeochemical cycles of carbon and nutrients due to the formation of intermediate & deep water and the sea ice carbon pump^{2–4}. Most of it is recognized as one of the largest high-nutrient low-chlorophyll (HNLC) regions with low biological productivity despite nutrient abundance in the ocean⁵. However, during the Last Glacial Maximum (LGM, ~25,000 years ago), an increase in biological production due to the supply of dust-derived iron in the SO may have reduced the atmospheric CO₂ concentration and contributed to global cooling, while the opposite may have occurred during interglacial periods⁶. Thus, it is important to clarify the net community production (NCP) in the SO for understanding the impact of ocean biological production on the Earth climate system.

Recently, in the SO, accelerated mass loss of the Antarctic ice sheet may have promoted ocean surface stratification, providing a suitable environment for biological production^{7,8}. The strengthening of ice sheet melting and calving of the Antarctic ice sheet may bring iron and increase biological production in SO⁹. Biological production in the SO may increase due to the combined effect of enhanced stratification and increased iron input, and consequently drawdown atmospheric CO₂ concentration^{6,10}. Therefore, to understand the future climate change, it is also essential to elucidate the spatiotemporal distribution of NCP in the SO, and anthropogenic CO₂ uptake in the ocean.

The ideal approach to estimate NCP is to (i) directly estimate the uptake and remineralization of dissolved inorganic carbon (DIC) in the ocean since the change in DIC is the most straightforward result of biological production and (ii) estimate it throughout the year since the uptake and remineralization of DIC are repeated on a yearly cycle due to the revolution of the Earth². On the other hand, climate change has had a great impact on the marine environment in recent decades^{1,2,7}. Therefore, it is furthermore necessary to (iii) clarify the change of NCP on a decadal scale to understand the changes in ocean biological production and its impact on climate. The existing mainstream approach for estimating the NCP is based on satellite and shipboard observations. Satellite observations estimate the detailed spatiotemporal distribution of biological production from sea surface chlorophyll-*a* concentrations with a constant carbon to chlorophyll-*a* ratio^{11,12}. However, satellite-based estimation of the NCP in the SO may be underestimated as satellites can only observe a depth of a few meters from the sea surface and cannot observe the subsurface chlorophyll-*a* maximum at a depth of tens of meters in the SO¹³. The shipboard observation of the NCP is based on methods that require stoichiometric ratios that are assumed to be constant over the entire ocean termed as the Redfield ratio¹⁴, including on-deck incubation oxygen¹⁵, nitrate distribution time-series¹⁶, and the carbon isotope mass balance method¹⁷. The advantage of shipboard observation is that it enables us to observe the subsurface chlorophyll-*a* maximum and estimate the NCP accurately¹⁸. However, there is a gap between the current state of research and the ideal state. Regarding (i) direct estimation of DIC, this is because of the lack of sensor technology for DIC, which makes continuous spatiotemporal observation of DIC difficult. Previous estimates of NCP have been based indirectly on continuous DIC data obtained by combining sensor-measured dissolved oxygen (DO) continuous data with a constant ratio of DO to DIC. This ratio is known to vary widely with NCP and remineralization, as well as with different values spatiotemporally. This introduces great uncertainty into the current method of estimating NCP. Furthermore, the severe climatic conditions and the impact of sea ice coverage on CO₂ outgassing in the SO make accurate DIC

observation more difficult. Regarding (ii) estimation through a year, the current situation in (i) makes it difficult to estimate the NCP throughout the year, when the uptake and remineralization periods are mixed because the ratio of DO to DIC for NCP and remineralization are different. For (iii) long-term estimation of NCP, it is currently difficult to estimate long-term NCP over the entire SO because of the spatiotemporal sparseness of observational data.

To break through the current situation, we attempted to utilize the parameterization technique to expand the data required to estimate the NCP and to reconstruct the DIC spatiotemporal distribution to estimate the NCP in the SO without using the stoichiometric ratio. Currently, several studies have been conducted using neural network models to predict DIC in the ocean and to estimate NCP from the predicted data^{19–22}. However, these neural network models are black boxes because they are difficult to show as equations, and it is hard to reproduce their estimates. Moreover, the selection of the input parameters in these previous studies is subjective and there are covariances between parameters, which brings uncertainties to these estimates. To overcome these shortcomings of the neural network model, we first developed a hybrid parameterization, which combines Multiple Linear Regression (MLR) and Neural Network (NN), for predicting DIC based on the high-accuracy hydrographic parameters of seawater temperature (T), salinity (S), DO, and water pressure (Pr) from the Global Ocean Data Analysis Project version 2 (GLODAPv2.2020) dataset²³ (see Method section “DIC Parameterization methods” for details). We then applied the MLR-NN hybrid parameterization to T, S, DO, and Pr measured by a large number of Biogeochemical Argo floats (BGC-Argo), which has a continuous 10–14 days cycle for approximately 6 years²⁴. Based on the change in reconstructed DIC above, we attempted to estimate the spatiotemporal high-resolution distribution of NCP along with an upward supply of remineralized carbon in the SO, wherein the seasonal decrease in DIC in the ocean surface water column was defined as NCP and the seasonal increase was defined as Restoration (RES) (see Method section “Estimation of NCP and RES” for details).

Results and discussion

DIC reconstruction in the SO. As described above, to obtain a spatiotemporal high-resolution distribution of DIC in the SO, it is essential to develop a DIC parameterization that can reconstruct the DIC concentration. We utilized our hybrid parameterization of DIC from T, S, DO, and Pr based on a back-propagation neural network model (see Fig. S2; also see Method section “DIC Parameterization methods”).

We used BGC-Argo data to obtain large amounts of T, S, DO, and Pr. Applying our hybrid parameterization of DIC to the T, S, DO, and Pr measured in 27,039 cycles of 154 BGC-Argos from 2004 to 2019, we obtained the spatiotemporal distribution of DIC over the SO (see Method section “Data used in this study” for details).

NCP and RES mapping in the SO. We obtained the spatiotemporal distributions of NCP and RES (upward supply of remineralized DIC from the deep to surface ocean) for the first time, encompassing the entire SO by combining the NN-based parameterization of DIC with BGC-Argo data (Fig. 1; see Method section “Estimation of NCP and RES” for details). We found that NCP is higher in the western parts of all sectors (> 4 mol C m⁻² year⁻¹, Fig. 1), including the western boundary of the Atlantic and Indian Oceans, as the upwelling caused by westerly winds may bring micronutrients such as iron from Patagonia, southern Australia, New Zealand, and some islands located in the westside of each sector to the surface ocean and fertilize the phytoplankton blooms in the SO^{25–27}. By extending the BGC-Argo data in Fig. 1

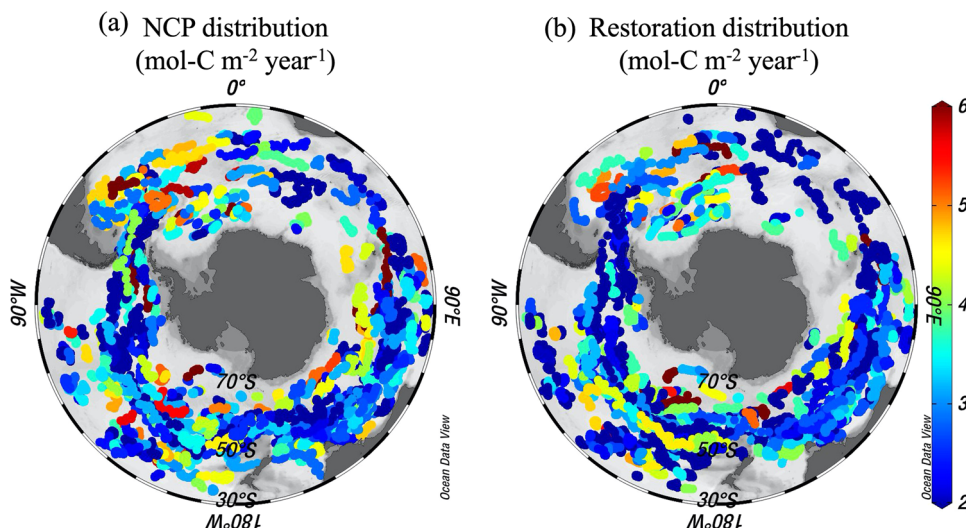


Fig. 1 Distribution of NCP ($\text{mol-C m}^{-2} \text{ year}^{-1}$) and RES ($\text{mol-C m}^{-2} \text{ year}^{-1}$) data of 154 BGC-Argo during 2004 - 2019. **a** Distribution of NCP. **b** Distribution of RES. Color dots indicate the observed data points through the BGC-Argo trajectories. These figures were drawn using Ocean Data View⁴⁹.

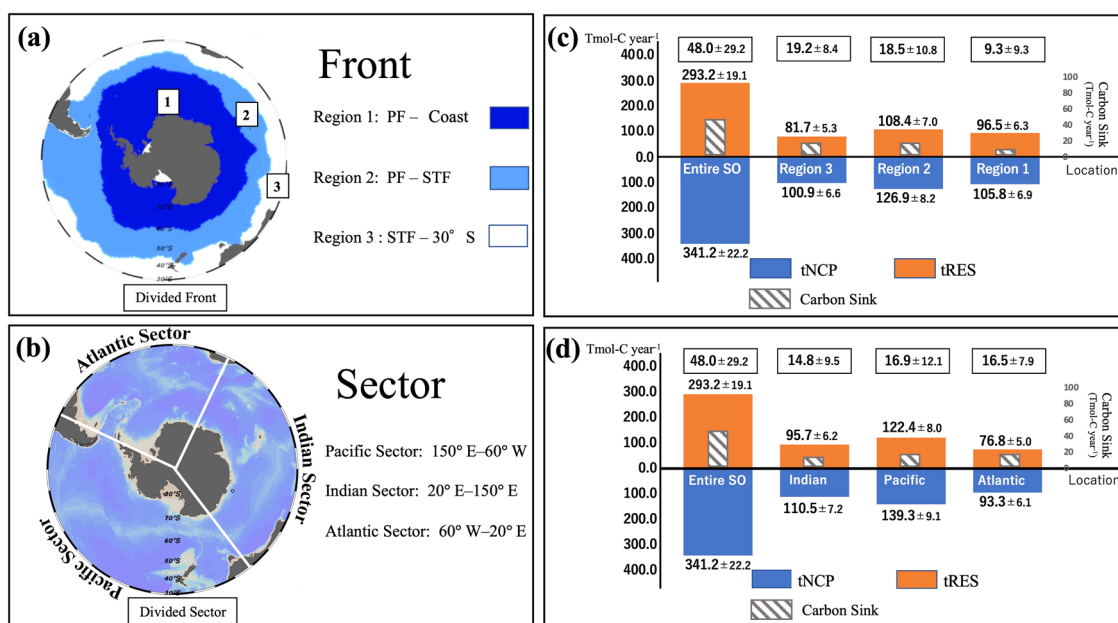


Fig. 2 Total NCP (tNCP, Tmol-C year^{-1}) and total Restoration (tRES, Tmol-C year^{-1}) for each front and sector in the SO. Blue and orange bars indicate tNCP and tRES, respectively. Note that the unit of carbon is Tmol-C ($= 0.012 \text{ Pg-C}$) in this figure. **a** Map of the SO is divided by the Subtropical (STF) and the Polar Front (PF). **b** Map of the SO is divided into three sectors: the Indian, Pacific, and Atlantic. **c** tNCP and tRES in the south of PF (Region 1, which is strongly affected by the sea ice⁷), the zone between PF and STF (Region 2), and the zone north of STF (Region 3) along with the entire SO. **d** tNCP and tRES in the Indian ($20^\circ \text{ E} - 150^\circ \text{ E}$), Pacific ($150^\circ \text{ E} - 60^\circ \text{ W}$), and the Atlantic sector ($60^\circ \text{ W} - 20^\circ \text{ E}$) along with the entire SO. The boxed numbers in the upper parts of Figs. 2c and 2d and the gray bars indicate the amount of Carbon Sink (CS, tNCP minus tRES) (Tmol-C year^{-1}). The tNCP and tRES were $341.2 \pm 22.2 \text{ Tmol-C year}^{-1}$ ($4.1 \pm 0.3 \text{ Pg-C year}^{-1}$) and $293.2 \pm 19.1 \text{ Tmol-C year}^{-1}$ ($3.5 \pm 0.2 \text{ Pg year}^{-1}$), respectively. The errors in c and d are 6.5%, while the CS error was calculated by the propagation of the error between tNCP and tRES (see section “4: Uncertainties of NCP, RES and CS” in Supplementary information for details).

to represent the entire SO (see Supplementary Note “3: Gridding of NCP and RES data” for details), we found that over the SO, the total NCP (tNCP, NCP multiplied by ocean surface area) reached $4.1 \pm 0.3 \text{ Pg-C year}^{-1}$ (remark: this value is equivalent to $341.2 \pm 22.2 \text{ Tmol-C year}^{-1}$; $\text{Tmol} = 10^{12} \text{ mol}$), which accounts for about 45% of the global ocean organic carbon export given by the previous study ($9.1 \pm 0.2 \text{ Pg-C year}^{-1}$)²⁸, and the total Restoration (tRES, RES multiplied by ocean surface area) reached $3.5 \pm 0.2 \text{ Pg-C year}^{-1}$ ($293.2 \pm 19.1 \text{ Tmol-C year}^{-1}$) (Fig. 2, Fig. S6). The uncertainties are estimated as 6.5% (see Supplementary Note “4:

Uncertainties of NCP, RES and CS” for details). The value of the NCP over the SO from 2004 to 2019 was generally ~20% larger than that of the NCP model simulations and primary production of the SO^{13,29,30} (Table 1). This difference may be derived from the consideration of subsurface chlorophyll-a maximum in our study using critical depth as the NCP integral depth and the application of DIC parameterization.

Contrastingly, the difference between tNCP and tRES ($0.6 \pm 0.3 \text{ Pg-C year}^{-1}$; generally, it is termed as “Removal,” which in this study, we also refer to as “carbon sink”(CS)) can be considered as

Table 1 Comparison of tNCP between this study and the previous studies.

| References | Method | Period | Location | tNCP (Pg-C year ⁻¹) |
|-----------------------|--|-----------|---------------|---------------------------------|
| This study | Neural network-based parameterization and BGC-Argo | 2004–2019 | South of 30°S | 4.1 ± 0.3 |
| Arteaga et al. (2018) | Carbon export efficiency models and satellite observation* | 2005–2016 | South of 30°S | 2.7 ± 0.6 *** |
| Arrigo et al. (2008) | Primary production from satellite observation* | 1997–2006 | South of 50°S | 1.9 ± 0.1 **** |
| Li et al. (2021) | VGPM, BGC-Argo and NCP model* | 1997–2020 | South of 35°S | 3.91 ± 0.16 |
| Chang et al. (2014) | Neural network-based self-organizing map (SOM)* | 1998–2009 | South of 30°S | 3.5 |
| Johnson et al. (2017) | Annual nitrate drawdown measured by BGC-Argo | 2009–2016 | South of 50°S | 1.3 |

* Satellite data-based method.

** The average tNCP of the previous studies in this table is 2.9 ± 1.2 Pg-C year⁻¹, and our estimate is about 20% larger than the average value of the previous studies.

*** Estimation of net primary production (NPP).

**** Estimation of gross primary production (GPP).

Table 2 Comparison of the regional amount of NCP and RES in each sector of the SO. The uncertainties in these estimations are 6.5%.

| Region | Location | Ocean surface area (10 ¹² m ²) | ^a NCP (mol-C m ⁻² year ⁻¹) | ^b RES (mol-C m ⁻² year ⁻¹) | ^c tNCP' (Tmol-C year ⁻¹) | ^d tRES' (Tmol-C year ⁻¹) |
|-----------------|---------------|---|--|--|---|---|
| SO | South of 30°S | 110 | 3.1 ± 0.2 | 2.7 ± 0.2 | 341 ± 22 | 297 ± 22 |
| Indian sector | 20°E– 150°E | 37 | 2.9 ± 0.2 | 2.7 ± 0.2 | 107 ± 7 | 100 ± 7 |
| Pacific sector | 150°E– 60°W | 47 | 2.9 ± 0.2 | 2.5 ± 0.2 | 136 ± 9 | 118 ± 9 |
| Atlantic sector | 60°W– 20°E | 26 | 3.6 ± 0.2 | 3.0 ± 0.2 | 93 ± 5 | 78 ± 5 |

^a NCP of unit area.^b RES of unit area.^c total NCP in each region, calculated by NCP of unit area multiplied by ocean surface area.^d total RES in each region, calculated by RES of unit area multiplied by ocean surface area.

the amount of carbon transported into the ocean interior, and this result is very close to the estimation of CO₂ net ocean uptake based on the atmospheric transport model in the SO south of 30°S, 0.53 ± 0.23 Pg-C year⁻¹³¹. Our estimate of CS in the SO accounts for a maximum of approximately 75% of the carbon sink in the global ocean (0.8 Pg-C year⁻¹)³², which may be caused by the transportation of water masses into the ocean interior, including Antarctic Intermediate (AAIW) and sub-Antarctic Mode Water (SAMW) in the SO³³.

Regional characteristics of NCP and RES in the SO. To characterize the NCP at the Polar Front zones and the basin scales, we divided the SO into three front zones³⁴ and three ocean sectors as follows: Region 1, the zone south of the polar front (PF); Region 2, the zone between the PF and the Subtropical Front (STF); Region 3, the zone north of the STF; Indian sector: 20–150°E; Pacific sector: 150°E–60°W; Atlantic sector: 60°W–20°E (Fig. 2). Higher tNCP was found in Region 2 due to the confluence of nutrient-rich sub-Antarctic waters with nutrient-poor subtropical waters and the mixing of cold and warm currents causing the seawater to mix up and down, interacting with westerly wind augmentation leading to sufficient nutrients³⁰. Similarly, there is a great amount of CS in Regions 2 and 3 (the area north of the PF), which may also be due to AAIW and SAMW bringing a large amount of carbon to the ocean interior^{33,35}. Conversely, despite having more nutrients than the other regions, Region 1 had a much lower CS (Fig. 2c). This may be due to the lower biological pumping activity caused by the longer ice cover period and iron limitation at high latitudes^{36,37}. As for each ocean sector, the Pacific has the highest tNCP, followed by the Indian, and the Atlantic has the lowest tNCP (Fig. 2d). However, the ranking of the three ocean sectors was reversed in terms of tNCP per unit area (Table 2). Despite the Atlantic Sector having the smallest area, there was a wide area with higher NCP (> 4 mol-C m⁻² year⁻¹) of all the ocean sectors, extending along the South American continent coast (Fig. 1 & Fig. S6), resulting in a larger

tNCP per unit area in the Atlantic Sector (Table 2). This is probably due to the supply of iron and other nutrients from the South American continent²⁶ and upwelling due to the Atlantic meridional overturning circulation².

To verify the accuracy of the NCP and RES gridding, we also computed tNCP and tRES for each sector and the entire SO by multiplying the NCP and RES average unit area by the ocean area (Table 2). We found that these values are essentially the same as the tNCP and tRES calculated by gridding (Fig. 2c, d), which proves the reliability of the tNCP and tRES obtained by gridding for the entire SO (Fig. S6).

Comparing our result with a previous study³⁸ about the meridional distribution of NCP in the SO despite only in the Indian sector, we found that the value of NCP in our study is in the same order as that in the previous study (Fig. S7). However, the previous study shows higher NCP in the low-latitude regions and no NCP in the high-latitude regions, which contrasts with the almost constant meridional NCP distribution in our study. The NCP in the previous study was derived from averaging approximately one-week observations in each season, with the observations concentrated in the Indian sector. In contrast, our results are derived from Argo's year-round observations, and are distributed over the entire SO. Considering the full-year NCP for the entire SO, our results may be more convincing.

Temporal variabilities of NCP and RES in the SO. To reveal the variations in the NCP of the SO over the past decades, we plotted the time series of the 3 years running mean of the NCP and RES in the SO from 2008 to 2017 (Fig. 3a). Since the BGC-Argo data before 2008 are not sufficient to cover the Southern Ocean, we have used only the data after 2008 to obtain more representative estimates of trends. Over the mid-SO (between 45°S and 60°S), which is controlled by strong westerlies and characterized by nutrient-rich deep water upwelling and intermediate water formation, we found a significant decrease of ~0.8% per year in the NCP and no significant trend in RES from 2008 to 2017 (Fig. 3a).

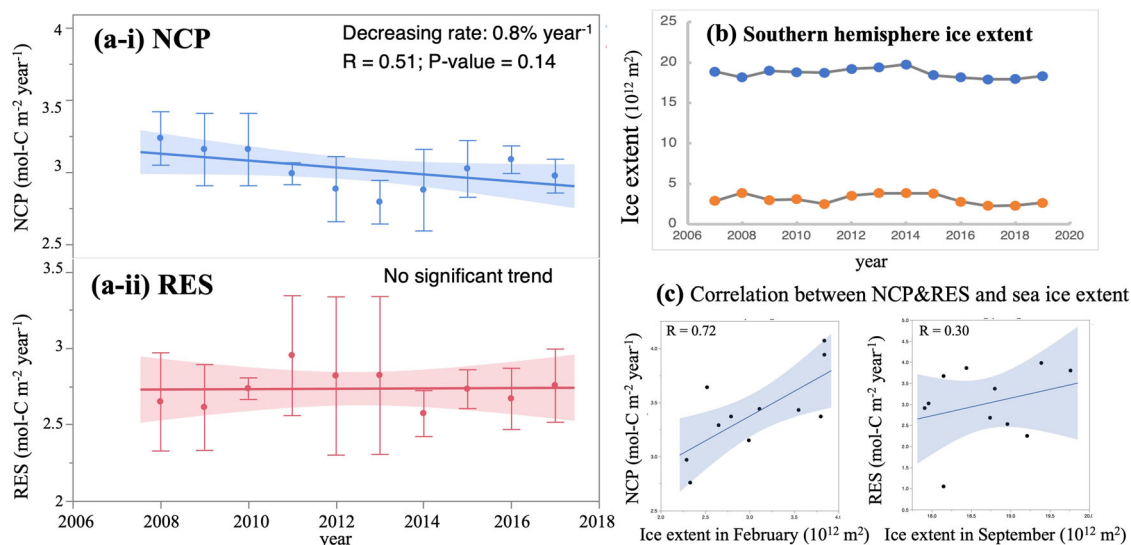


Fig. 3 Time-series of NCP, RES, and sea ice extent in the SO. **a** Time-series of averaged NCP and RES ($\text{mol-C m}^{-2} \text{ year}^{-1}$) over the mid-SO from 2008 to 2017; NCP and RES are depicted in 3 years running mean. Data used to estimate the time series are depicted in Fig. S4. **b** Interannual variation of sea ice extents in September and February (10^{12} m^2) for the southern hemisphere from 2007 to 2019 from Parkinson [2019]⁴¹. **c** Correlation between sea ice extent and NCP, RES in the SO from 2008 to 2018. The horizontal axes depict sea ice extent for the month corresponding to NCP and RES period. Note that the sea ice extent data in February is shifted one year to the previous year. In **a**, **c**, the line and the shaded area represent the linear relationship between the variables and the 95% confidence interval, respectively. The error bars indicate one standard deviation. However, because of the spatial bias of data for each year, especially in the coastal regions, the error may be larger. Note: In the previous study based on the neural network model and Argo floats (2015–2020)²¹, the trend of NCP south of 35°S of about $-0.1\% \text{ year}^{-1}$ was estimated by the assumption that the average DIC was $2100 \mu\text{mol year}^{-1}$ in the mixed layer and the DIC was totally consumed by NCP. However, this neural network model is a black box because they are difficult to show as equations, and it is hard to reproduce their estimate. Moreover, the selection of the input parameters in this previous study is subjective and there are covariances between parameters, which brings uncertainties to these estimates.

This decreasing trend in the NCP is opposite to the increasing trend during LGM⁶. During the LGM, the drying of the air due to global cooling and the northward shift of westerlies in the southern hemisphere transported terrestrial-derived dust into the ocean, leading to iron fertilization and an increase in marine biological production in the SO, which resulted in the drawdown of atmospheric CO_2 by approximately 80 ppm lower than the modern preindustrial average⁶. Conversely, modern SO is predominantly affected by global warming and the southward shift of the westerlies, leading to accelerated melting of glaciers in the coastal region with a shallower mixed layer and limited upwelling of nutrients, which consequently causes a decreasing trend in biological production in the mid SO^{6,7,39}.

On the other hand, iron released from the melting sea ice may have broader impacts on the biological production in the SO⁴⁰, and temporal variability of ice extent may affect the NCP in the SO widely. We compared the time series of NCP between 45°S and 60°S and the time series of February and September sea ice extents for the Southern Hemisphere⁴¹, although the ice extent does not reach this latitude range. There were correlations between sea ice extent and NCP in the SO (Fig. 3c), suggesting that the decrease in sea ice extent causes seawater environment changes, including ocean freshening, intensified ocean stratification, and reduction in iron supply from sea ice, which could potentially result in changes in the biology of the phytoplankton community and reduce biological production efficiency³⁹. Contrastingly, the correlation between RES and sea ice extent during September is because during the winter season, the mixing layer is deeper throughout the SO⁴², and deep winter mixing caused a large amount of DIC to upwell from the ocean interior, consequently leading to a weak correlation of RES with the Southern Hemisphere sea ice extent in the SO. Therefore, the significant decrease of 0.8% per year in the NCP in the mid-SO may be caused by feedback to the westerly southward

shift and stronger ocean stratification⁷. RES demonstrated no significant trend from 2008 to 2017. The new finding of a declining trend in NCPs in this study could indicate a reduction in CS as an anthropogenic carbon sink in the ocean, potentially accelerating future global warming and consequently altering the ocean biogeochemical cycle. As a caveat in estimating the time series, it should be noted that the NCP and RES trends may contain several decadal oscillations⁴³. Therefore, long-term and more extensive observations over several decades using BGC-Argo will be required in the future to determine the significance of this trend.

Our new concept in this study first constructed an MLR-NN hybrid parameterization for DIC in the SO and gave a simultaneous estimate of the spatiotemporal distributions of NCP, RES, and CS over the SO based on BGC-Argo observations, without relying on an idealized stoichiometry ratio. Furthermore, with the development of BGC-Argo in the global ocean, our method can be applied to the rest of the global ocean, leading to a deeper and better understanding of biological production and the change in the carbon budget under climate change in the global ocean now and in the future.

Methods

Data used in this study. The BGC-Argo data (T, S, DO, and Pr) used for constructing the spatiotemporal high-resolution mapping of DIC were sourced from the Japan Agency for Marine-Earth Science and Technology (JAMSTEC) Argo website (http://www.jamstec.go.jp/ARGO/argo_web/argo/) of the SO (south of 30°S) from 2004 to 2019. Information on BGC-Argo, wherein we utilized the data, is depicted in Fig. S3 and Table S1.

Due to the BGC-Argo DO sensor drift, it was essential to correct the BGC-Argo DO data to the high-accuracy shipboard DO observational data. We utilized the monthly World Ocean Atlas 2018 (WOA18)⁴⁴ dataset as the high-accuracy shipboard

DO and S observational data to compare with BGC-Argo DO and S data at depths below the mixed layer (the mixed layer depth is estimated when the temperature gradient from the surface exceeds $0.5\text{ }^{\circ}\text{C}$)⁴⁵ to 2000 m. We used the latitude and longitude of each BGC-Argo measurement cycle to determine WOA18 DO and S data at the corresponding location (latitude and longitude $\pm 0.5^{\circ}$) to determine a linear relationship. As a result, the linear relationship between WOA18 and S in BGC-Argo had a coefficient of determination of 0.99 or higher, thus verifying that it was not required to correct S for this BGC-Argo. For this BGC-Argo, if the coefficient of determination of DO was greater than 0.8 between WOA18 and BGC-Argo, we corrected the DO based on the linear relationship with the WOA18 DO data to use it for DIC estimation. Additionally, if the BGC-Argo measurement period was less than two years, we did not use it because of the difficulty in obtaining the annual periodicity of DIC. We obtained 154 valid BGC-Argo data with the above steps and then standardized it according to the WOA18 data depth levels (see Supplementary Note “1: Data standardization” for details).

In addition, there is a further point that must be considered. The increase in anthropogenic CO_2 leads to a decrease in atmospheric oxygen concentration (maximum of 4 ppm year^{-1})⁴⁶, leading to a possible temporal difference between the WOA18 and BGC-Argo DO data. Thus, it is necessary to check the effect of anthropogenic CO_2 on the DO in the ocean. The WOA18 DO data are climatological data based on observations from 1955 to 2017 (the median year is 1986), and the BGC-Argo data used were from 2004 to 2019 (the median year was 2013). The 27-year difference in the period between the WOA18 and BGC-Argo data used here ($2013-1986=27$) resulted in a decrease in atmospheric oxygen concentration of 108 ppm, equivalent to 0.05% of the current atmospheric oxygen concentration ($\sim 209,000\text{ ppm}$). Oxygen solubility is higher when temperatures and salinity are lower. To estimate the maximum effect of anthropogenic CO_2 on the DO, we assumed a water temperature of $-1.8\text{ }^{\circ}\text{C}$ (around the freezing temperature of seawater) and salinity of 34 (near the Antarctica coast) in the SO, this reduction in the atmospheric oxygen concentration would lead to a decrease of $0.2\text{ }\mu\text{mol kg}^{-1}$ (0.05%) of the maximum saturated oxygen concentration of $370\text{ }\mu\text{mol kg}^{-1}$. However, the precision of the GLODAPv2.2020 DO data used in our construction of DIC parameterization is $\sim 1\%$ ²³, which would lead to an error of approximately $4\text{ }\mu\text{mol kg}^{-1}$ for the maximum saturated oxygen concentration. Therefore, the reduction in the maximum saturated oxygen concentration caused by the reduction in oxygen concentration during the 27-year difference in the period between the WOA18 and BGC-Argo data could be neglected when compared to the error in the GLODAPv2 DO data.

DIC Parameterization methods. As biological productivity in the SO consumes DIC in seawater, we can treat this consumed DIC during the production period as NCP. We first constructed DIC parameterization for the SO as follows:

We used an MLR-NN hybrid method to construct the DIC parameterization (Fig. S1a). The MLR method is a useful approach used to estimate the SO DIC⁷. As the MLR method relies strongly on linear relationships with parameters to estimate DIC, it is suitable for DIC estimation in the ocean interior where the environment is relatively stable. However, it is difficult for the MLR method to estimate DIC in many locations in the surface mixed layer where biological and physical processes are complex, and the linear relationships are difficult to maintain. Therefore, using the MLR method to reconstruct the DIC of the surface mixed layer constraints must be imposed on the parameters^{7,47} (Table S2). Contrastingly, the NN method can provide extensive DIC estimates

without considering the constraints (see Supplementary Note “2: Introduction of DIC parameterization methods” for details). However, it is difficult for the NN method to evaluate the covariance between each input parameter. To evaluate whether each parameter could be applied to DIC parameterization, we first constructed an MLR parameterization for DIC (Fig. S2a), considered parameters with an F-value (an index used in linear regression to test the significance of parameter) greater than 2.4 as significant, and verified the presence of multicollinearity between each parameter using the variance inflation factor (VIF)⁷. As a result, we obtained valid parameters including T, S, and Pr to reflect physical processes and apparent oxygen utilization (AOU) to reflect biological processes, where AOU is calculated from DO and saturated DO concentration⁴⁸. Next, using the NN method (the back-propagation neural network model) with CTD-bottle data of T, S, DO, and Pr since 2000 from the GLODAPv2.2020 dataset (Fig. S2b), we constructed NN-based parameterization of DIC over the SO (see Equation S2 for details). When comparing the root mean square error (RMSE) between the MLR and MLR-NN methods, although the MLR-NN method RMSE is slightly larger than that of the MLR method (Fig. S2), the back-propagation model of the NN model can effectively reconstruct the DIC over the SO, including the surface mixed layer. This MLR-NN hybrid parameterization can be used to reconstruct DIC in terms of T, S, DO, and Pr from 0 m to the deepest depth ($\sim 2000\text{ m}$) measurable by BGC-Argo. Around Antarctica, the predicted DIC derived from BGC-Argo data were in great agreement with the GLODAP DIC observations within the RMSE of our parameterization (Fig. S8). Using the amount of DIC decrease during the production period, we can quantify the amount of NCP from the SO (see the next section, “Estimation of NCP and RES” for details).

Estimations of NCP and RES. To obtain the NCP and RES by applying MLR-NN hybrid DIC parameterization to the BGC-Argo data, we set standard depth levels (5, 10, 20, 30, 40, 50, 60, 70, 80, 90, 100, 125, 150, 175, and 200 m; see Supplementary Note “1: Data standardization” for details), and obtained spatiotemporal high-resolution distribution of DIC at each depth over the SO.

In this study, to obtain the NCP and RES in the water column, we first utilized the seawater temperature (T) at 30 m depth as a benchmark to delineate the production and restoration period (production period: the period from the annual minimum DIC (DIC_{\min}) to the annual maximum DIC (DIC_{\max}); restoration period: the period from DIC_{\max} to DIC_{\min})¹¹. NCP in each standard layer is defined as the decrease from DIC_{\max} to DIC_{\min} , and RES in each standard layer is defined as the increase from DIC_{\min} to DIC_{\max} . We computed the DIC variation for each standard depth level during the Production and Restoration periods. We then integrated the total DIC variation within the water column during the Production and Restoration periods. The NCP integration depth level is determined by the critical depth, where the amount of DIC variation is zero, defined as the depth at which the integrated phytoplankton production balances the integrated destruction in the surface mixed layer rather than the mixed layer depth used in previous studies^{13,30} (see the schematic in Figs. S5 and S9). For RES, the integration depth level was the same as that of the NCP. Note that the NCP and RES estimated in this study are defined by the net change in DIC in each period and may be apparent values. As the BGC-Argo cannot move autonomously and the flow motion is almost the same as that of seawater (Lagrangian motion), we assume that the data collected by the same BGC-Argo are approximately in the same water column.

Our method can account for NCP at the SCM that are unobservable to satellites, which leads to potentially more significant

tNCP values in our study than in previous studies^{13,29,30,48} (see Table 1). However, we may not be able to obtain hydrographic data (T, S, DO, and Pr) from BGC-Argo for the Antarctic continental coast and areas where BGC-Argo has not floated due to the bathymetry of the SO coast and sea ice limitations²⁴. Here, we use the Weight Average algorithm to expand the NCP and restore these regions using Ocean Data View⁴⁹. To generate a spatiotemporal high-resolution distribution of NCP and RES in the SO, all reconstructed NCP and RES data were extended to a common 1° × 1° latitude-longitude grid south of 30°S (see Supplementary Note “3: Gridding of NCP and RES data” for details). However, compared with in situ NCP observations^{30,39,48}, the weighted average algorithm in this study may have uncertainty along the Antarctic coast because of the inability to measure some regions of high biological production along the Antarctic coast due to the measurement limitations of BGC-Argo.

Data availability

The GLODAP dataset used to construct DIC parameterization was sourced from <https://glodap.info/>. The BGC-Argo dataset was sourced from the Japan Agency for Marine-Earth Science and Technology (JAMSTEC) Argo website (http://www.jamstec.go.jp/ARGO/argo_web/argo/). The WOA dataset used to correct the Argo DO was sourced from <https://www.ncei.noaa.gov/products/world-ocean-atlas>. Predicted DIC and NCP, RES estimations data of this study can be downloaded from <https://doi.org/10.6084/m9.figshare.24311710.v1>.

Code availability

The parameterizations in this study were constructed by using JMP13 software (https://www.jmp.com/en_gb/home.html).

Received: 4 April 2023; Accepted: 23 October 2023;

Published online: 18 December 2023

References

1. Khatiwala, S. et al. Global ocean storage of anthropogenic carbon. *Biogeosciences* **10**, 2169–2191, <https://doi.org/10.5194/bg-10-2169-2013> (2013).
2. Sarmiento, J. L. & Gruber, N. *Ocean Biogeochemical Dynamics*. (Princeton University Press, 2006).
3. Sarmiento, J. L., Gruber, N., Brzezinski, M. A. & Dunne, J. P. High-latitude controls of thermocline nutrients and low latitude biological productivity. *Nature* **427**, 56–60, <https://doi.org/10.1038/nature02127> (2004).
4. Takahashi, T. et al. Global sea–air CO₂ flux based on climatological surface ocean pCO₂, and seasonal biological and temperature effects. *Deep-Sea Res. II: Top. Stud. Oceanogr.* **49**, 1601–1622, [https://doi.org/10.1016/S0967-0645\(02\)00003-6](https://doi.org/10.1016/S0967-0645(02)00003-6) (2002).
5. Boyd, P. W. et al. Mesoscale iron enrichment experiments 1993–2005: synthesis and future directions. *Science* **315**, 612–617, <https://doi.org/10.1126/science.1131669> (2007).
6. Sigman, D. M. & Boyle, E. A. Glacial/interglacial variations in atmospheric carbon dioxide. *Nature* **407**, 859–869, <https://doi.org/10.1038/35038000> (2000).
7. Pan, X. L., Li, B. F. & Watanabe, Y. W. Intense ocean freshening from melting glacier around the Antarctica during early twenty-first century. *Sci. Rep.* **12**, 383, <https://doi.org/10.1038/s41598-021-04231-6> (2022).
8. Shadwick, E. H., Tilbrook, B. & Currie, K. I. Late-summer biogeochemistry in the Mertz Polynya: East Antarctica. *J. Geophys. Res.* **122**, 7380–7394, <https://doi.org/10.1002/2017jc013015> (2017).
9. Duprat, L. P. A. M., Bigg, G. R. & Wilton, D. J. Enhanced Southern Ocean marine productivity due to fertilization by giant icebergs. *Nat. Geosci.* **9**, 219–221, <https://doi.org/10.1038/ngeo2633> (2016).
10. Martinez-Garcia, A. et al. Iron fertilization of the Subantarctic ocean during the last ice age. *Science* **343**, 1347–1350, <https://doi.org/10.1126/science.1246848> (2014).
11. Behrenfeld, M. J. & Falkowski, P. G. Photosynthetic rates derived from satellite-based chlorophyll concentration. *Limnol. Oceanogr.* **42**, 1–20, <https://doi.org/10.4319/lo.1997.42.1.0001> (1997).
12. Arrigo, K. R., van Dijken, G. L. & Bushinsky, S. Primary production in the Southern Ocean, 1997–2006. *J. Geophys. Res.* **113**, <https://doi.org/10.1029/2007jc004551> (2008).
13. Li, Z., Lozier, M. S. & Cassar, N. Linking Southern Ocean mixed-layer dynamics to net community production on various timescales. *J. Geophys. Res.* **126**, <https://doi.org/10.1029/2021jc017537> (2021).
14. Anderson, L. A. & Sarmiento, J. L. Redfield ratios of remineralization determined by nutrient data analysis. *Glob. Biogeochem. Cycles* **8**, 65–80, <https://doi.org/10.1029/93gb03318> (1994).
15. Bender, M. et al. A comparison of four methods for determining planktonic community production. *Limnol. Oceanogr.* **32**, 1085–1098, <https://doi.org/10.4319/lo.1987.32.5.1085> (1987).
16. MacCreedy, P. & Quay, P. Biological export flux in the Southern Ocean estimated from a climatological nitrate budget. *Deep-Sea Res. II: Top. Stud. Oceanogr.* **48**, 4299–4322, [https://doi.org/10.1016/S0967-0645\(01\)00090-x](https://doi.org/10.1016/S0967-0645(01)00090-x) (2001).
17. Quay, P. D., Stutsman, J., Feely, R. A. & Juranek, L. W. Net community production rates across the subtropical and equatorial Pacific Ocean estimated from air–sea δ¹³C disequilibrium. *Global Biogeochem. Cycles* **23**, n/a–n/a, <https://doi.org/10.1029/2008gb003193> (2009).
18. Baldry, K., Strutton, P. G., Hill, N. A. & Boyd, P. W. Subsurface Chlorophyll-a Maxima in the Southern Ocean. *Front. Mar. Sci.* **7**, <https://doi.org/10.3389/fmars.2020.00671> (2020).
19. Bittig, H. C. et al. Oxygen Optode Sensors: Principle, Characterization, Calibration, and Application in the Ocean. *Front. Mar. Sci.* **4**, <https://doi.org/10.3389/fmars.2017.00429> (2018).
20. Keppler, L., Landschützer, P., Gruber, N., Lauvset, S. K. & Stemmler, I. Seasonal Carbon Dynamics in the Near-Global Ocean. *Global Biogeochem. Cycles* **34**, <https://doi.org/10.1029/2020gb006571> (2020).
21. Keppler, L., Landschützer, P., Lauvset, S. K. & Gruber, N. Recent Trends and Variability in the Oceanic Storage of Dissolved Inorganic Carbon. *Global Biogeochem. Cycles* **37**, <https://doi.org/10.1029/2022gb007677> (2023).
22. Sauzède, R. et al. Estimates of water-column nutrient concentrations and carbonate system parameters in the Global Ocean: a novel approach based on neural networks. *Front. Mar. Sci.* **4**, <https://doi.org/10.3389/fmars.2017.00128> (2017).
23. Olsen, A. et al. GLODAPv2.2019 – an update of GLODAPv2. *Earth Syst. Sci. Data* **11**, 1437–1461, <https://doi.org/10.5194/essd-11-1437-2019> (2019).
24. Bittig, H. C. et al. A BGC-Argo guide: planning, deployment, data handling and usage. *Front. Mar. Sci.* **6**, <https://doi.org/10.3389/fmars.2019.00502> (2019).
25. Graham, R. M., De Boer, A. M., van Sebille, E., Kohfeld, K. E. & Schlosser, C. Inferring source regions and supply mechanisms of iron in the Southern Ocean from satellite chlorophyll data. *Deep-Sea Res. Part I: Oceanogr. Res. Papers* **104**, 9–25, <https://doi.org/10.1016/j.dsr.2015.05.007> (2015).
26. Johnson, K. S., Chavez, F. P. & Friederich, G. E. Continental-shelf sediment as a primary source of iron for coastal phytoplankton. *Nature* **398**, 697–700, <https://doi.org/10.1038/19511> (1999).
27. Paparazzo, F. et al. Patagonian dust as a source of macronutrients in the Southwest Atlantic ocean. *Oceanogr.* **31**, 33–39, <https://doi.org/10.5670/oceanog.2018.408> (2018).
28. DeVries, T. & Weber, T. The export and fate of organic matter in the ocean: New constraints from combining satellite and oceanographic tracer observations. *Global Biogeochem. Cycles* **31**, 535–555, <https://doi.org/10.1002/2016gb005551> (2017).
29. Arteaga, L., Haëntjens, N., Boss, E., Johnson, K. S. & Sarmiento, J. L. Assessment of export efficiency equations in the Southern ocean applied to satellite-based net primary production. *J. Geophys. Res.* **123**, 2945–2964, <https://doi.org/10.1002/2018jc013787> (2018).
30. Chang, C. H., Johnson, N. C. & Cassar, N. Neural network-based estimates of Southern Ocean net community production from in situ O₂/Ar and satellite observation: a methodological study. *Biogeosciences* **11**, 3279–3297, <https://doi.org/10.5194/bg-11-3279-2014> (2014).
31. Long, M. C. et al. Strong Southern Ocean carbon uptake evident in airborne observations. *Science* **374**, 1275–1280, <https://doi.org/10.1126/science.abi4355> (2021).
32. Landschützer, P., Gruber, N. & Bakker, D. C. E. Decadal variations and trends of the global ocean carbon sink. *Global Biogeochem. Cycles* **30**, 1396–1417, <https://doi.org/10.1002/2015gb005359> (2016).
33. Sabine, C. L. et al. The oceanic sink for anthropogenic CO₂. *Science* **305**, 367–371, <https://doi.org/10.1126/science.1097403> (2004).
34. Chapman, C. C., Lea, M.-A., Meyer, A., Sallée, J.-B. & Hindell, M. Defining Southern Ocean fronts and their influence on biological and physical processes in a changing climate. *Nat. Clim. Change* **10**, 209–219, <https://doi.org/10.1038/s41558-020-0705-4> (2020).
35. Gruber, N. et al. The oceanic sink for anthropogenic CO₂ from 1994 to 2007. *Science* **363**, 1193–1199, <https://doi.org/10.1126/science.aau5153> (2019).
36. Henley, S. F. et al. Changing Biogeochemistry of the Southern Ocean and Its Ecosystem Implications. *Front. Mar. Sci.* **7**, <https://doi.org/10.3389/fmars.2020.00581> (2020).
37. Moore, C. M. et al. Processes and patterns of oceanic nutrient limitation. *Nat. Geosci.* **6**, 701–710, <https://doi.org/10.1038/ngeo1765> (2013).

38. Cassar, N. et al. The Southern Ocean biological response to aeolian iron deposition. *Science* **317**, 1067–1070, <https://doi.org/10.1126/science.1144602> (2007).
39. Lin, Y. et al. Decline in plankton diversity and carbon flux with reduced sea ice extent along the Western Antarctic Peninsula. *Nat. Commun.* **12**, 4948, <https://doi.org/10.1038/s41467-021-25235-w> (2021).
40. Alderkamp, A.-C. et al. Iron from melting glaciers fuels phytoplankton blooms in the Amundsen Sea (Southern Ocean): Phytoplankton characteristics and productivity. *Deep-Sea Res. II: Top. Stud. Oceanogr.* **71–76**, 32–48, <https://doi.org/10.1016/j.dsr2.2012.03.005> (2012).
41. Parkinson, C. L. A 40-y record reveals gradual Antarctic sea ice increases followed by decreases at rates far exceeding the rates seen in the Arctic. *Proc Natl Acad Sci USA* **116**, 14414–14423, <https://doi.org/10.1073/pnas.1906556116> (2019).
42. Gordon, A. L. & Huber, B. A. Southern ocean winter mixed layer. *J. Geophys. Res.* **95**, <https://doi.org/10.1029/JC095iC07p11655> (1990).
43. Watanabe, Y. W., Li, B. F. & Wakita, M. Long-Term Trends of Direct and Indirect Anthropogenic Effects on Changes in Ocean pH. *Geophys. Res. Lett.* **45**, 9106–9113, <https://doi.org/10.1029/2018gl078084> (2018).
44. García, H. E. et al. World Ocean Atlas 2018, Volume 3: dissolved oxygen, apparent oxygen utilization, and oxygen saturation. *A. Mishonov Technical Ed. NOAA Atlas NESDIS* **83**, 38 (2019).
45. de Boyer Montégut, C. Mixed layer depth over the global ocean: an examination of profile data and a profile-based climatology. *J. Geophys. Res.* **109**, <https://doi.org/10.1029/2004jc002378> (2004).
46. Langenfelds, R. L. et al. Partitioning of the global fossil CO₂ sink using a 19-year trend in atmospheric O₂. *Geophys. Res. Lett.* **26**, 1897–1900, <https://doi.org/10.1029/1999gl900446> (1999).
47. Pan, X. L., Li, B. F. & Watanabe, Y. W. The Southern Ocean with the largest uptake of anthropogenic nitrogen into the ocean interior. *Sci. Rep.* **10**, 8838, <https://doi.org/10.1038/s41598-020-65661-2> (2020).
48. Johnson, K. S., Plant, J. N., Dunne, J. P., Talley, L. D. & Sarmiento, J. L. Annual nitrate drawdown observed by SOCCOM profiling floats and the relationship to annual net community production. *J. Geophys. Res.* **122**, 6668–6683, <https://doi.org/10.1002/2017jc012839> (2017).
49. Schlitzer, R. *Ocean Data View*, <https://odv.awi.de> (2020).

Acknowledgements

We are grateful to K. Yamauchi for processing a large amount of BGC-Argo data. We also acknowledge Y. Nakano and K. Sato of the Japan Agency for Marine-Earth Science and Technology (JAMSTEC) for providing BGC-Argo data. This study was partially supported by the Ministry of Education, Culture, Sports, Science, and Technology, Japan (grant number KAKEN JP22H05003, JP21J12486).

Author contributions

Conceptualization: X.L.P., X.X.L. and Y.W.W. Methodology: X.L.P., X.X.L. and Y.W.W. Investigation: X.L.P., X.X.L. Visualization: X.L.P., X.X.L. Funding acquisition: X.L.P. and Y.W.W. Project administration: Y.W.W. Supervision: Y.W.W. Writing—original draft: X.L.P., X.X.L. and Y.W.W. Writing—review & editing: X.L.P., X.X.L., R.M., D.H. and Y.W.W.

Competing interests

The authors declare no competing interests.

Additional information

Supplementary information The online version contains supplementary material available at <https://doi.org/10.1038/s43247-023-01067-y>.

Correspondence and requests for materials should be addressed to Xianliang L. Pan.

Peer review information *Communications Earth & Environment* thanks Maria Vernet, Angela Kuhn-Cordova and the other, anonymous, reviewer(s) for their contribution to the peer review of this work. Primary Handling Editors: José Luis Iriarte Machuca, Clare Davis. A peer review file is available.

Reprints and permission information is available at <http://www.nature.com/reprints>

Publisher's note Springer Nature remains neutral with regard to jurisdictional claims in published maps and institutional affiliations.



Open Access This article is licensed under a Creative Commons Attribution 4.0 International License, which permits use, sharing, adaptation, distribution and reproduction in any medium or format, as long as you give appropriate credit to the original author(s) and the source, provide a link to the Creative Commons licence, and indicate if changes were made. The images or other third party material in this article are included in the article's Creative Commons licence, unless indicated otherwise in a credit line to the material. If material is not included in the article's Creative Commons licence and your intended use is not permitted by statutory regulation or exceeds the permitted use, you will need to obtain permission directly from the copyright holder. To view a copy of this licence, visit <http://creativecommons.org/licenses/by/4.0/>.

© The Author(s) 2023